Supporting Information

A general strategy to enhance electrochemical activity and energy density of energy-storage materials through using sintering aids with redox activity: a case study of $Mo_4Nb_{26}O_{77}$

*Songjie Li, Jiazhe Gao, Yinjun Ou, Wenze Wang, Qian Zhang, Shangfu Gao, Xuehua Liu, Chunfu Lin**

Institute of Materials for Energy and Environment, School of Materials Science and Engineering, Qingdao University, Qingdao 266071, China

* *Corresponding author. E-mail address: linchunfu@qdu.edu.cn.*

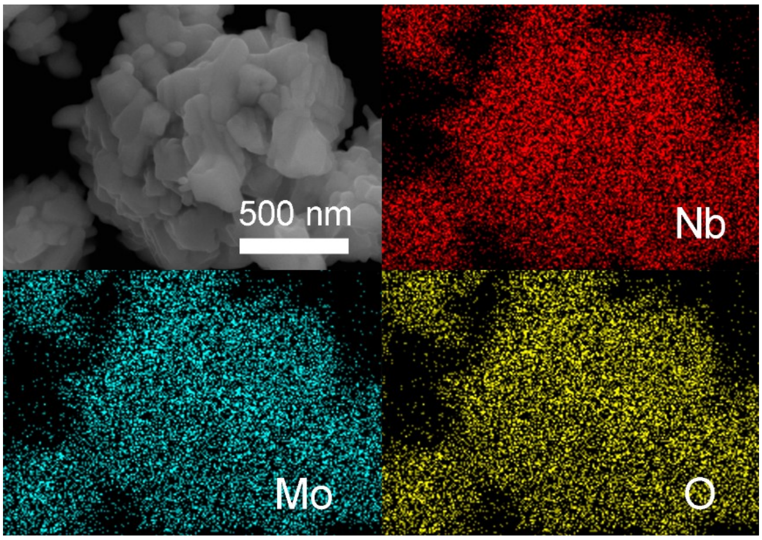

Fig. S1. EDX mapping images of $Mo_4Nb_{26}O_{77}$ submicron-sized particles.

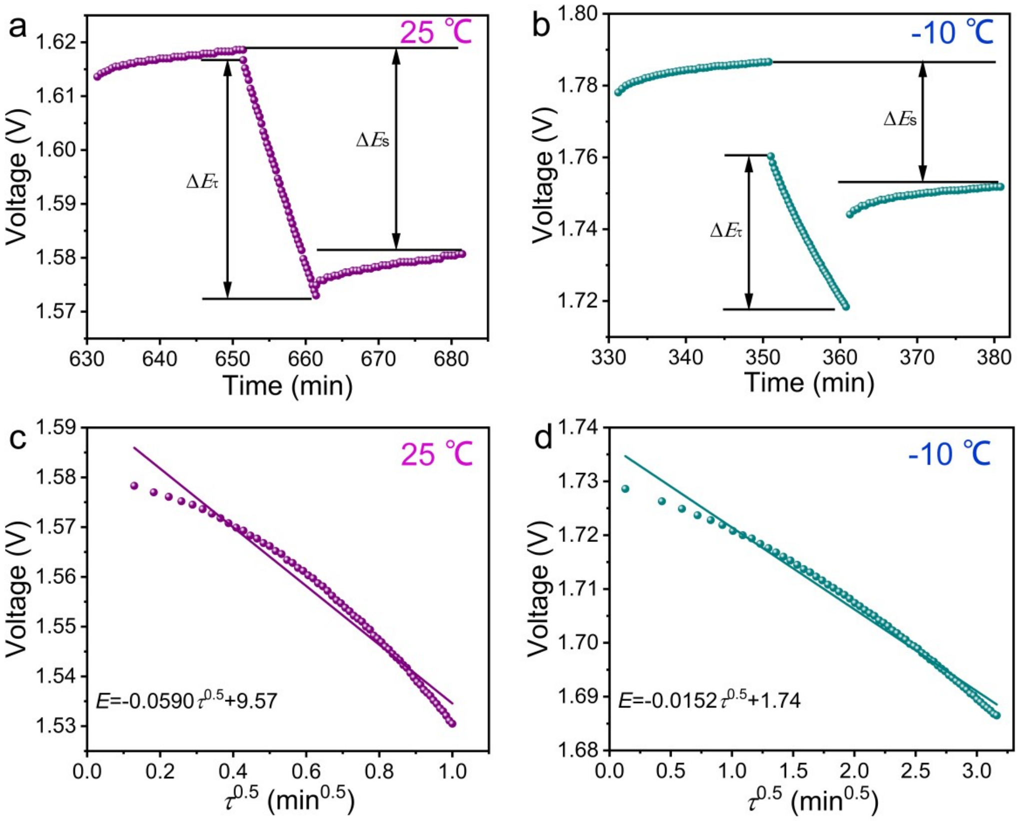

Fig. S2. *E* versus *t* curves for a single step in GITT experiment of $Mo_4Nb_{26}O_{77}$ submicron-sized particles at a) 25 and b) −10 °C. Linear behavior of *E* versus $\tau^{0.5}$ relationship during a typical titration in $Mo_4Nb_{26}O_{77}$ submicron-sized particles at c) 25 and d) −10 °C.

Calculations of apparent Li^+ diffusion coefficients of $Mo_4Nb_{26}O_{77}$ submicron-sized particles from GITT

The GITT test is conducted on the $Mo_4Nb_{26}O_{77}$/Li cell to study the Li^+ diffusivity in the $Mo_4Nb_{26}O_{77}$ submicron-sized particles. Fig. 5d and Fig. 5e respectively exhibit the typical GITT curves of the $Mo_4Nb_{26}O_{77}$ submicron-sized particles at 25 and −10 °C during the first two lithiation–delithiation cycles. For a clear observation, a single step of GITT is presented in Fig. S2a/Fig. S2b. Based on the Fick's second law, the apparent Li^+ diffusion coefficients (D_{Li}) of the $Mo_4Nb_{26}O_{77}$ submicron-sized particles can be calculated by using Eq. S1 [S1]:

$$D_{Li} = \frac{4}{\pi}\left(\frac{m_b V_m}{M_b S}\right)^2 \left(\frac{\Delta E_s}{\tau\left(dE_\tau / d\sqrt{\tau}\right)}\right)^2 \qquad \left(\tau \ll \frac{L^2}{D_{Li}}\right) \tag{S1}$$

where, M_B is the molar mass of $Mo_4Nb_{26}O_{77}$, V_m is the molar volume of $Mo_4Nb_{26}O_{77}$, m_B is the mass of $Mo_4Nb_{26}O_{77}$, S is the $Mo_4Nb_{26}O_{77}$ electrode area, τ is the pulse duration time, L is the $Mo_4Nb_{26}O_{77}$ electrode thickness, and ΔE_s and ΔE_τ respectively represent the change in the equilibrium potential and the change in potential during the current pulse, which can be gained from the GITT curves (Fig. S2a and Fig. S2b). As the potential during a single titration delivers a linear relationship with $\tau^{0.5}$ (Fig. S2c/Fig. S2d), Eq. S1 can be simplified as Eq. S2:

$$D_{Li} = \frac{4}{\pi\tau}\left(\frac{m_b V_m}{M_b S}\right)^2 \left(\frac{\Delta E_s}{\Delta E_\tau}\right)^2 \qquad \left(\tau \ll \frac{L^2}{D_{Li}}\right) \tag{S2}$$

Based on Eq. S2, the apparent Li^+ diffusion coefficients of the $Mo_4Nb_{26}O_{77}$ submicron-sized particles during different states of discharge/charge at 25 and −10 °C are obtained, and displayed in Fig. 5d and Fig. 5e, respectively.

Table S1. Results of crystal analysis by Rietveld refinement in $Mo_4Nb_{26}O_{77}$ submicron-sized particles (monoclinic) with *C*2 space group, and the comparisons with shear ReO_3-type niobate anode materials previously reported. Interlayer spacings (usually *b* values) are highlighted in red.

material	*a* (Å)	*b* (Å)	*c* (Å)	*α*, *γ* (°)	*β* (°)	*V* (Å^3)	reference
$Mo_4Nb_{26}O_{77}$	**29.76355 (87)**	**3.82011 (10)**	**26.00112 (27)**	**90**	**92.377 (4)**	**2953.788 (86)**	**this work**
$V_3Nb_{17}O_{50}$	20.36708 (85)	3.79885 (15)	11.89108 (55)	90	127.227 (3)	794.945 (68)	[S2]
$MoNb_{12}O_{33}$	22.7931 (6)	3.82094 (1)	17.72972 (5)	90	123.3 (1)	1261.021 (60)	[S3]
$ZrNb_{14}O_{37}$	29.87123 (255)	3.82209 (26)	21.16379 (157)	90	95.078 (7)	2406.798 (430)	[S4]
$TiNb_2O_7$	20.36708 (85)	3.79885 (15)	11.89108 (55)	90	127.227 (3)	794.945 (68)	[S5]
$Ti_2Nb_{10}O_{29}$	15.52368 (58)	3.8112 (2)	20.5382 (13)	90	113.042 (5)	1117.67 (15)	[S6]
$Al_{0.5}Nb_{24.5}O_{62}$	29.9005 (72)	3.8228 (7)	21.1950 (45)	90	95.079 (3)	2413.20 (92)	[S7]
$Cr_{0.5}Nb_{24.5}O_{62}$	29.91514 (299)	3.82628 (32)	21.15166 (201)	90	94.944 (8)	2412.092 (488)	[S8]
$Ga_{0.5}Nb_{24.5}O_{62}$	30.02809 (53)	3.83409 (52)	21.10826 (35)	90	96.041 (1)	2416.709 (927)	[S9]
$W_5Nb_{16}O_{55}$	21.0209 (9)	3.8241 (6)	23.0822 (15)	90	126.489 (3)	1689.60 (71)	[S10]
$Fe_{0.5}Nb_{24.5}O_{62}$	29.7203 (61)	3.81813 (70)	21.1036 (44)	90	95.352 (17)	2383.807 (22)	[S11]
$FeNb_{11}O_{29}$	28.70490 (49）	3.82569 (7)	20.62376 (42)	90	90	2264.822 (60)	[S12]

$Mg_2Nb_{34}O_{87}$	15.60459 (13)	3.83071 (2)	20.64403 (13)	90	113.096 (6)	1135.119 (161)	[S13]
$Zn_2Nb_{34}O_{87}$	28.71489 (11)	3.82780 (2)	20.65497 (8)	90	90	2270.295 (252)	[S14]
$HfNb_{24}O_{62}$	29.92508 (125)	3.82525 (14)	21.21133 (87)	90	95.068 (5)	2418.588 (167)	[S15]
$Cu_2Nb_{34}O_{87}$	15.59868 (130)	3.83115 (21)	20.64336 (127)	90	113.063 (6)	1135.059 (161)	[S16]
$TiNb_{24}O_{62}$	29.79212 (173)	3.81751 (20)	21.09986 (114)	90	95.018 (5)	2390.526 (288)	[S17]
$AlNb_{11}O_{29}$	15.55789 (85)	3.81126 (16)	20.53599 (94)	90	113.303 (4)	1118.354 (112)	[S18]
$Ni_2Nb_{34}O_{87}$	28.69691 (89)	3.84015 (10)	20.66244 (65)	90	90	2277.011 (167)	[S19]

Table S2. Fractional atomic parameters of $Mo_4Nb_{26}O_{77}$ with *C*2 space group.

atom	*x*	*y*	*z*	occupancy	site
Mo0	0.241455	0.25	0.208689	1	4*c*
Mo1	0.044892	0	0.402234	0.0714	4*c*
Mo2	0.000051	0	0.267343	0.0714	4*c*
Mo3	0.163318	0	0.364353	0.0714	4*c*
Mo4	0.119995	0	0.211033	0.0714	4*c*
Mo5	0.103080	0.5	0.126194	0.0714	4*c*
Mo6	0.297897	0.5	0.489506	0.0714	4*c*
Mo7	0.261218	0.5	0.362641	0.0714	4*c*
Mo8	0.220645	0.5	0.075442	0.0714	4*c*
Mo9	0.417929	0.5	0.450245	0.0714	4*c*
Mo10	0.378183	0.5	0.308527	0.0714	4*c*
Mo11	0.348898	0	0.198761	0.0714	4*c*
Mo12	0.322672	0	0.063135	0.0714	4*c*
Mo13	0.475458	0	0.153464	0.0714	4*c*
Mo14	0.435190	0	0.010244	0.0714	4*c*
Nb1	0.044892	0	0.402234	0.9286	4*c*
Nb2	0.000051	0	0.267343	0.9286	4*c*
Nb3	0.163318	0	0.364353	0.9286	4*c*
Nb4	0.119995	0	0.211033	0.9286	4*c*
Nb5	0.103080	0.5	0.126194	0.9286	4*c*
Nb6	0.297897	0.5	0.489506	0.9286	4*c*
Nb7	0.261218	0.5	0.362641	0.9286	4*c*

Nb8	0.220645	0.5	0.075442	0.9286	4*c*
Nb9	0.417929	0.5	0.450245	0.9286	4*c*
Nb10	0.378183	0.5	0.308527	0.9286	4*c*
Nb11	0.348898	0	0.198761	0.9286	4*c*
Nb12	0.322672	0	0.063135	0.9286	4*c*
Nb13	0.475458	0	0.153464	0.9286	4*c*
Nb14	0.435190	0	0.010244	0.9286	4*c*
O1	0.042151	0.5	0.396852	1	4*c*
O2	0.024205	0.5	0.276908	1	4*c*
O3	0.183166	0.5	0.427164	1	4*c*
O4	0.117909	0.5	0.199559	1	4*c*
O5	0.114728	0	0.141137	1	4*c*
O6	0.265402	0	0.480783	1	4*c*
O7	0.237360	0	0.338012	1	4*c*
O8	0.242202	0	0.054041	1	4*c*
O9	0.452829	0	0.533580	1	4*c*
O10	0.371951	0	0.284647	1	4*c*
O11	0.357913	0.5	0.231246	1	4*c*
O12	0.250903	0.5	0.967210	1	4*c*
O13	0.487261	0.5	0.189643	1	4*c*
O14	0.435192	0.5	0.024738	1	4*c*
O15	0.068435	0	0.495137	1	4*c*
O16	0.025816	0	0.336439	1	4*c*
O17	0.109759	0	0.380804	1	4*c*

O18	0.065048	0	0.239667	1	4*c*
O19	0.026597	0.5	0.071694	1	4*c*
O20	0.186482	0	0.445039	1	4*c*
O21	0.156227	0	0.295537	1	4*c*
O22	0.080046	0.5	0.059826	1	4*c*
O23	0.200337	0	0.189223	1	4*c*
O24	0.174512	0.5	0.111398	1	4*c*
O25	0.272478	0.5	0.410938	1	4*c*
O26	0.220674	0.5	0.269220	1	4*c*
O27	0.349337	0.5	0.455336	1	4*c*
O28	0.296349	0.5	0.311371	1	4*c*
O29	0.286910	0	0.244647	1	4*c*
O30	0.248892	0.5	0.165363	1	4*c*
O31	0.208702	0.5	0.016111	1	4*c*
O32	0.394930	0.5	0.368914	1	4*c*
O33	0.324526	0	0.133060	1	4*c*
O34	0.405329	0.5	0.387880	1	4*c*
O35	0.433904	0.5	0.304792	1	4*c*
O36	0.407042	0	0.188796	1	4*c*
O37	0.364448	0	0.058755	1	4*c*
O38	0.449247	0	0.089317	1	4*c*
O39	0	0.5	0	1	2*a*

Table S3. Sintering temperature and BET specific surface area of $Mo_4Nb_{26}O_{77}$ submicron-sized particles, and the comparisons with previously-reported niobate anode materials from solid-state reaction.

niobate	sintering temperature (°C)	BET specific surface area ($m^2\ g^{-1}$)	reference
$Mo_4Nb_{26}O_{77}$	**700**	**3.3**	**this work**
$V_3Nb_{17}O_{50}$	1000	0.9	[S2]
$MoNb_{12}O_{33}$	1000	0.5	[S3]
$ZrNb_{14}O_{37}$	1050	1.6	[S4]
$TiNb_2O_7$	1100	0.8	[S5]
$Ti_2Nb_{10}O_{29}$	1150	1.3	[S6]
$Al_{0.5}Nb_{24.5}O_{62}$	1150	0.6	[S7]
$Cr_{0.5}Nb_{24.5}O_{62}$	1150	0.7	[S8]
$Ga_{0.5}Nb_{24.5}O_{62}$	1150	1.5	[S9]
$W_5Nb_{16}O_{55}$	1150	1.7	[S10]
$Fe_{0.5}Nb_{24.5}O_{62}$	1150	0.7	[S11]
$FeNb_{11}O_{29}$	1200	0.9	[S12]
$Mg_2Nb_{34}O_{87}$	1200	0.5	[S13]
$Zn_2Nb_{34}O_{87}$	1200	0.6	[S14]
$HfNb_{24}O_{62}$	1200	0.8	[S15]
$Cu_2Nb_{34}O_{87}$	1200	0.5	[S16]
$TiNb_{24}O_{62}$	1250	0.7	[S17]
$AlNb_{11}O_{29}$	1300	0.9	[S18]
$Ni_2Nb_{34}O_{87}$	1350	unreaveled	[S19]

Table S4. Theoretical and practical capacities of $Mo_4Nb_{26}O_{77}$ submicron-sized particles as well as the reversible capacity below 1.5 V at 0.1C, and the comparisons with previously-reported niobate anode materials from solid-state reaction.

niobate	theoretical capacity (mAh g^{-1})	practical capacity (mAh g^{-1})	practical-to-theoretical capacity ratio (%)	capacity below 1.5 V at 0.1C (mAh g^{-1})	reference
$Mo_4Nb_{26}O_{77}$	**399**	**366**	**91.7**	**149**	**this work**
$V_3Nb_{17}O_{50}$	423	281	66.4	127	[S2]
$MoNb_{12}O_{33}$	400	298	74.5	140	[S3]
$ZrNb_{14}O_{37}$	378	246	63.6	125	[S4]
$TiNb_2O_7$	387	268	69.3	139	[S5]
$Ti_2Nb_{10}O_{29}$	396	279	70.5	125	[S6]
$Al_{0.5}Nb_{24.5}O_{62}$	400	264	66.0	130	[S7]
$Cr_{0.5}Nb_{24.5}O_{62}$	398	291	73.1	130	[S8]
$Ga_{0.5}Nb_{24.5}O_{62}$	397	272	68.5	140	[S9]
$W_5Nb_{16}O_{55}$	356	243	68.3	128	[S10]
$Fe_{0.5}Nb_{24.5}O_{62}$	398	247	62.1	140	[S11]
$FeNb_{11}O_{29}$	400	286	71.5	130	[S12]
$Mg_2Nb_{34}O_{87}$	396	293	73.9	140	[S13]
$Zn_2Nb_{34}O_{87}$	389	301	77.4	135	[S14]
$HfNb_{24}O_{62}$	366	256	69.9	110	[S15]
$Cu_2Nb_{34}O_{87}$	389	311	79.9	135	[S16]
$TiNb_{24}O_{62}$	388	301	77.5	135	[S17]
$AlNb_{11}O_{29}$	389	294	75.6	125	[S18]
$Ni_2Nb_{34}O_{87}$	392	339	86.5	130	[S19]

Table S5. Comparisons of apparent Li^+ diffusion coefficients (D_{Li}) of $Mo_4Nb_{26}O_{77}$ submicron-sized particles with previously-reported niobate anode materials from solid-state reaction.

material	D_{Li} ($cm^2\ s^{-1}$)	test method	reference
$Mo_4Nb_{26}O_{77}$	**1.9×10^{-11} (25 °C)**	**GITT**	**this work**
$Mo_4Nb_{26}O_{77}$	**8.9×10^{-12} (–10 °C)**	**GITT**	**this work**
$V_3Nb_{17}O_{50}$	3.24×10^{-14} (25 °C)	GITT	[S2]
$MoNb_{12}O_{33}$	3.57×10^{-12} (25 °C)	GITT	[S3]
$ZrNb_{14}O_{37}$	6.28×10^{-13} (25 °C)	CV	[S4]
$TiNb_2O_7$	5.17×10^{-15} (25 °C)	GITT	[S5]
$Ti_2Nb_{10}O_{29}$	6.9×10^{-13} (25 °C)	GITT	[S6]
$Al_{0.5}Nb_{24.5}O_{62}$	8.02×10^{-12} (25 °C)	GITT	[S7]
$Cr_{0.5}Nb_{24.5}O_{62}$	6.5×10^{-12} (25 °C)	GITT	[S8]
$Ga_{0.5}Nb_{24.5}O_{62}$	4.9×10^{-12} (25 °C)	GITT	[S9]
$W_5Nb_{16}O_{55}$	4.57×10^{-14} (25 °C)	CV	[S10]
$Fe_{0.5}Nb_{24.5}O_{62}$	1.21×10^{-12} (25 °C)	GITT	[S11]
$FeNb_{11}O_{29}$	$1.6\sim1.7\times10^{-12}$ (25 °C)	GITT	[S12]
$Mg_2Nb_{34}O_{87}$	8.28×10^{-12} (25 °C)	GITT	[S13]
$Zn_2Nb_{34}O_{87}$	5.9×10^{-12} (25 °C)	GITT	[S14]
$HfNb_{24}O_{62}$	1.51×10^{-13} (25 °C)	GITT	[S15]
$Cu_2Nb_{34}O_{87}$	3.5×10^{-13} (25 °C)	GITT	[S16]
$TiNb_{24}O_{62}$	7.4×10^{-12} (25 °C)	GITT	[S17]
$AlNb_{11}O_{29}$	2.39×10^{-13} (25 °C)	CV	[S18]
$Ni_2Nb_{34}O_{87}$	5.8×10^{-13} (25 °C)	GITT	[S19]

References

[S1] A.J. Bard, L.R. Faulkner, Electrochemical Methods: Fundamentals and Applications, second ed., Wiley, New York, 2001.

[S2] Q. Fu, X. Zhu, R. Li, G. Liang, L. Luo, Y. Chen, Y. Ding, C. Lin, K. Wang, X. Zhao, A low-strain $V_3Nb_{17}O_{50}$ anode compound for superior Li^+ storage, Energy Storage Mater. 30 (2020) 401–411.

[S3] X. Zhu, J. Xu, Y. Luo, Q. Fu, G. Liang, L. Luo, Y. Chen, C. Lin, X. Zhao, $MoNb_{12}O_{33}$ as a new anode material for high-capacity, safe, rapid and durable Li^+ storage: structural characteristics, electrochemical properties and working mechanisms, J. Mater. Chem. A 7 (2019) 6522–6532.

[S4] Y. Li, R. Zheng, H. Yu, X. Cheng, T. Liu, N. Peng, J. Zhang, M. Shui, J. Shu, Observation of $ZrNb_{14}O_{37}$ nanowires as a lithium container via in-situ and ex-situ techniques for high-performance lithium-ion batteries, ACS Appl. Mater. Interfaces 11 (2019) 22429–22438.

[S5] L. Hu, C. Lin, C. Wang, C. Yang, J. Li, Y. Chen, S. Lin, $TiNb_2O_7$ nanorods as a novel anode material for secondary lithium-ion batteries, Funct. Mater. Lett. 6 (2016) 1642004.

[S6] T. Takashima, T. Tojo, R. Inada, Y. Sakurai, Characterization of mixed titanium-niobium oxide $Ti_2Nb_{10}O_{29}$ annealed in vacuum as anode material for lithium-ion battery, J. Power Sources 276 (2015) 113–119.

[S7] Q. Fu, R. Li, X. Zhu, G. Liang, L. Luo, Y. Chen, C. Lin, X. Zhao, Design, synthesis and lithium-ion storage capability of $Al_{0.5}Nb_{24.5}O_{62}$, J. Mater. Chem. A 7 (2019) 19862–

19871.

[S8] C. Yang, S. Yu, C. Lin, F. Lv, S. Wu, Y. Yang, W. Wang, Z. Zhu, J. Li, N. Wang, S. Guo, $Cr_{0.5}Nb_{24.5}O_{62}$ nanowires with high electronic conductivity for high-rate and long-life lithium-ion storage, ACS Nano 11 (2017) 4217–4224.

[S9] R. Li, Y. Pu, J. Xu, Q. Fu, G. Liang, X. Zhu, L. Luo, Y. Chen, C. Lin, Novel $GaNb_{49}O_{124}$ microspheres with intercalation pseudocapacitance for ultrastable lithium-ion storage, Ceram. Int. 45 (2019) 12211–12217.

[S10] X. Ma, X. Cao, Y. Ye, F. Qiao, M. Qian, Y. Wei, Y. Wu, Z. Zi, J. Dai, Study on low-temperature performances of $Nb_{16}W_5O_{55}$ anode for lithium-ion batteries, Solid State Ionics 353 (2020) 115376.

[S11] R. Zheng, Y. Li, H. Yu, T. Liu, M. Xia, X. Zhang, N. Peng, J. Zhang, Y. Bai, J. Shu, Rational construction and decoration of $Fe_{0.5}Nb_{24.5}O_{62-x}$@C nanowires as superior anode material for lithium storage, Chem. Eng. J. 384 (2020) 123314.

[S12] X. Lou, C. Lin, Q. Luo, J. Zhao, B. Wang, J. Li, Q. Shao, X. Guo, N. Wang, Z. Guo, Crystal structure modification enhanced $FeNb_{11}O_{29}$ for lithium-ion batteries, ChemElectroChem 4 (2017) 3171–3180.

[S13] X. Zhu, Q. Fu, L. Tang, C. Lin, J. Xu, G. Liang, R. Li, L. Luo, Y. Chen, $Mg_2Nb_{34}O_{87}$ porous microspheres for use in high-energy, safe, fast-charging, and stable lithium-ion batteries, ACS Appl. Mater. Interfaces 10 (2018) 23711–23720.

[S14] X. Zhu, H. Cao, R. Li, Q. Fu, G. Liang, Y. Chen, L. Luo, C. Lin, X. Zhao, Zinc niobate materials: crystal structures, energy-storage capabilities and working mechanisms, J. Mater. Chem. A 7 (2019) 25537–25547.

[S15] Q. Fu, H. Cao, G. Liang, L. Luo, Y. Chen, V. Murugadoss, S. Wu, T. Ding, C. Lin, Z. Guo, A highly Li^+-conductive $HfNb_{24}O_{62}$ anode material for superior Li^+ storage, Chem. Commun. 56 (2020) 619–622.

[S16] L. Yang, X. Zhu, X. Li, X. Zhao, K. Pei, W. You, X. Li, Y. Chen, C. Lin, R. Che, Conductive copper niobate: superior Li^+-storage capability and novel Li^+-transport mechanism, Adv. Energy Mater. 9 (2019) 1902174.

[S17] C. Yang, S. Deng, C. Lin, S. Lin, Y. Chen, J. Li, H. Wu, Porous $TiNb_{24}O_{62}$ microspheres as high-performance anode materials for lithium-ion batteries of electric vehicles, Nanoscale 8 (2016) 18792–18799.

[S18] X. Lou, R. Li, X. Zhu, L. Luo, Y. Chen, C. Lin, H. Li, X. Zhao, New anode material for lithium-ion batteries: aluminum niobate ($AlNb_{11}O_{29}$), ACS Appl. Mater. Interfaces 11 (2019) 6089–6096.

[S19] C. Lv, C. Lin, X. S. Zhao, Rational design and synthesis of nickel niobium oxide with high-rate capability and cycling stability in a wide temperature range, Adv. Energy Mater. 12 (2022) 2102550.